Development of Pan-Anti-SARS-CoV-2 Agents through Allosteric Inhibition of nsp14/nsp10 Complex

Jingxin Chen, Ying Zhou, Xueying Wei, Xiaohan Xu, Zhenzhi Qin, Chon Phin Ong, Zi-Wei Ye, Dong-Yan Jin, Bernard Boitrel, Shuofeng Yuan, et al.

Development of Pan-Anti-SARS-CoV-2 Agents through Allosteric Inhibition of nsp14/nsp10 Complex

Jingxin Chen,[†] Ying Zhou,[†] Xueying Wei,[†,‡] Xiaohan Xu,[†] Zhenzhi Qin,[‡] Chon Phin Ong,[§] Zi-Wei Ye,[§] Dong-Yan Jin,[§] Bernard Boitrel,[//] Shuofeng Yuan,[‡] Jasper F.-W. Chan,[‡] Hongyan Li,[*,†] and Hongzhe Sun[*,†]

† Department of Chemistry, State Key Laboratory of Synthetic Chemistry and CAS-HKU Joint Laboratory of Metallomics on Health and Environment, The University of Hong Kong, Pokfulam Road, Pokfulam, Hong Kong 999077, P. R. China

‡ Department of Microbiology, The University of Hong Kong, Sassoon Road, Pokfulam, Hong Kong 999077, P. R. China

§ School of Biomedical Sciences, The University of Hong Kong, Sassoon Road, Pokfulam, Hong Kong 999077, P. R. China

// University of Rennes, CNRS, ISCR (Institut des Sciences Chimiques de Rennes)-UMR 6226, Rennes 35000, France

* Email: hylichem@hku.hk

* Email: hsun@hku.hk

ABSTRACT

SARS-CoV-2 nsp14 functions both as an exoribonuclease (ExoN) together with its critical cofactor nsp10 and as an S-adenosyl methionine-dependent (guanine-N7) methyltransferase (MTase), which

makes it an attractive target for the development of pan-anti-SARS-CoV-2 drugs. Herein, we screened a panel of compounds (and drugs) and found that certain compounds, especially, Bi(III)-based compounds could allosterically inhibit both MTase and ExoN activities of nsp14 potently. We further demonstrated that Bi(III) binds to both nsp14 and nsp10, resulting in the release of Zn(II) ions from the enzymes, as well as alternation of protein quaternary structures. The in vitro activities of the compounds were also validated in SARS-CoV-2-infected mammalian cells. Importantly, we showed that nsp14 serves as an authentic target of Bi(III)-based antivirals in SARS-CoV-2-infected mammalian cells by quantification of both the protein and inhibitor. This study highlights the importance of nsp14/nsp10 as a potential target for the development of pan-antivirals against SARS-CoV-2 infection.

KEYWORDS: *antiviral; bioinorganic chemistry; bismuth; nsp14 Exon and MTase; SARS-CoV-2*

SARS-CoV-2 has posed an unprecedented threat to public health worldwide, leading to over 765 million confirmed cases and 6.92 million deaths by the end of April 2023.[1] Despite different types of vaccines having been and are being developed, the COVID-19 pandemic still cannot be fully controlled until now owing to rapid mutation of the virus, leading to enhanced transmissibility and reduced sensitivity to vaccine-induced protection. Therefore, it is imperative to develop novel broad-spectrum anti-SARS-CoV-2 drugs to inhibit the replication and infection of the virus and its variants.

Metal-based agents are an attractive class of drugs with many therapeutic applications,[2] including platinum- or arsenic-based anticancer drugs,[3, 4] bismuth-based antiulcer drugs,[5-7] and gold-based antirheumatoid drugs.[8] Metal complexes are also increasingly recognized as a promising source for new antibiotics to deal with antimicrobial resistance.[9, 10] Different from organic compounds, which have been extensively screened or under development for antivirals,[11] the potential of metal-based compounds as antivirals is largely unexplored. Only recently, metal-based strategies for combating COVID-19 pandemic are being actively investigated.[12-18] Metal-based drugs often function through multitargeted modes of action,[5, 19, 20] which very much resembles the cocktail therapy used for the treatment of viral infection such as

HIV.[21, 22] Therefore, metal-based compounds might serve as a unique and new source of broad-spectrum antivirals.

We have previously demonstrated that clinically used bismuth antiulcer drugs, i.e., ranitidine bismuth citrate (RBC, Pylorid) and colloidal bismuth subcitrate (CBS, De-Nol) as well as other bismuth complexes exhibited comparable anti-SARS-CoV-2 activity to that of remdesivir, the first drug approved by the U. S. FDA as an emergency treatment of COVID-19 both in infected cells and in the golden Syrian hamster model.[13] Combinatorial *N*-acetyl-L-cysteine (NAC), a thiol-containing drug, with bismuth drugs (e.g., CBS) broadly suppressed the replication of a panel of medically important coronaviruses including MERS-CoV, hCoV-229E and SARS-CoV-2 Alpha variant (B.1.1.7) in the virus infected cells and an animal model through oral administration.[15] Importantly, bismuth-based therapies are currently in clinical trials. For example, BSS (Pepto-Bismol) is in a phase IV clinical trial (NCT04811339), and the combination therapy consisting of a bismuth-based drug (e.g., BSS) and a thiolate-containing drug (NAC) is currently in a phase II/III clinical trial in Hong Kong (CT0096/2022). In spite of the success of bismuth-based antivirals, the molecular mechanism of action is incompletely understood. The enzyme-based assays showed that bismuth drugs inhibited the activities of SARS-CoV-2 nsp13 (helicase) ,[13, 16] as well as the two proteases, i.e., main protease and papain-like protease.[15] However, it remains elusive whether bismuth-based antivirals also target other viral proteins/enzymes and what the authentic targets of bismuth drugs in the virus-infected mammalian cells.

The SARS-CoV-2 genome encodes 14 open reading frames (ORFs), of which ORF1a and ORF1b encode 16 nonstructural proteins (nsp), which play critical roles in viral transcription and replication as well as evasion of the host immune response, and are potential targets for the design of antiviral drugs.[23, 24] The SARS-CoV-2 nsp14 functions as an exoribonuclease (ExoN) and an S-adenosyl methionine-dependent (guanine-N7) methyltransferase (N7-MTase). The N-terminal ExoN domain of nsp14 plays a significant excision role in improving RNA synthesis fidelity and decreasing the lethal mutagenesis by removing mismatched nucleotides or nucleotide analogs at the 3'-end of RNA.[25] The C-terminal domain of nsp14 shows great N7-guanine MTase activity to assemble the cap structure at the 5' end of the virus

mRNA.[26] In SARS-CoV-2, nsp10 is a critical cofactor of nsp14 as it facilitates the formation of the ExoN active site, thus stimulating the ExoN activity of nsp14 remarkably.[27] Given the dual enzymatic activity of nsp14, together with its close interaction with the cofactor nsp10, nsp14/nsp10 complex might serve as an attractive target of anti-SARS-CoV-2 drugs.[28-30] Both nsp10 and nsp14 contain two and three zinc fingers, respectively. Based on the amino acid sequence alignment (Figure S1), the residues involved in the formation of these zinc fingers are highly conserved among several coronaviruses. Thus, specifically targeting the zinc fingers of the nsp14/nsp10 complex may allow broad-spectrum antiviral drugs to be developed.

Herein, we screened a series of compounds against the nsp14/nsp10 complex at an enzymatic level and found that certain compounds, especially Bi(III) compounds, exhibited comparable or better inhibitory activity to a series of clinically used antiviral drugs on both MTase and ExoN activities of nsp14, with IC_{50} values at a micromolar level. We demonstrated that Bi(III) compounds allosterically inhibited the nsp14/nsp10 enzymatic activity through the displacement of Zn(II) ions from the enzymes by Bi(III) ions, leading to quaternary structures being disrupted. The *in vitro* activities of the compounds at an enzymatic level were further confirmed in SARS-CoV-2-infected mammalian cells. Importantly, for the first time, we validated nsp14 as an authentic target of Bi(III)-based antivirals in SARS-CoV-2-infected mammalian cells. The importance of nsp14/nsp10 as an antiviral drug target was discussed.

Results and Discussion

Metal-Based Compounds Inhibit the MTase and ExoN Activities of nsp14/nsp10. Metal-based drugs or compounds often function through binding and inhibiting key proteins/ enzymes, thus interfering with key biological pathways.[20, 31] Recently, bismuth and gold drugs were demonstrated to inhibit zinc-containing resistant enzymes, e.g., metallo-β-lactamase (or MCR-1), through the displacement of their zinc cofactors, thus serving as antibiotic adjuvants for combating antimicrobial resistance.[32, 33] Moreover, bismuth drugs have also been shown to exert potent anti-SARS-CoV-2 efficacy both *in vitro* and in an animal model owing to targeting key zinc-containing enzymes such as helicase;[13, 15] however, it is not

clear whether bismuth and other potential metal-based anti-SARS-CoV-2 agents also target nsp14, thus perturbing the transcription and replication of SARS-CoV-2.

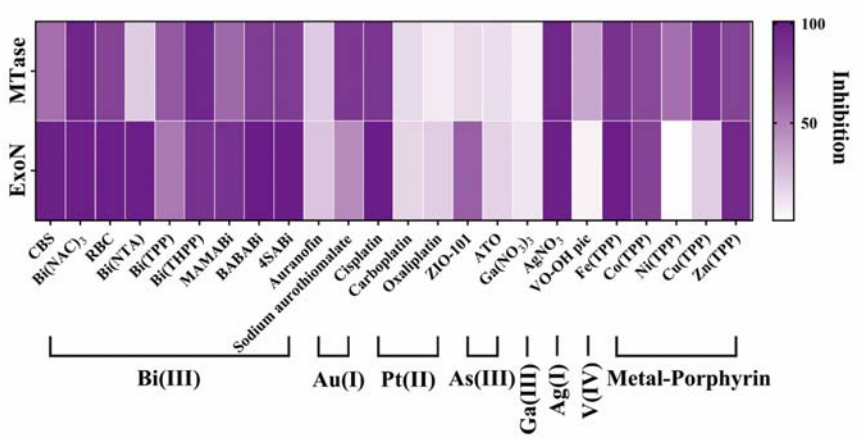

Figure 1. SARS-CoV-2 nsp14/nsp10 as a potential target of metal-based compounds against SARS-CoV-2. Percentages of inhibition on methyltransferase and exoribonuclease activity of nsp14 by metal-based compounds (n = 3). The concentrations used are 1 μM and 200 nM for nsp14 and 50 and 10 μM for metal compounds for methyltransferase and exoribonuclease activity assays, respectively.

To address this, we first overexpressed and purified full-length proteins of nsp10 and nsp14 and then evaluated whether metal compounds could serve as inhibitors of nsp14. The purity and identities of the recombinant proteins were verified by sodium dodecyl-sulfate polyacrylamide gel electrophoresis (SDS-PAGE) and liquid chromatography-mass spectrometry (LC-MS) after trypsin digestion (Figure S2). The recombinant nsp14 showed both MTase and ExoN activities (Figure S3). The MTase activity was monitored by MTase-Glo Methyltransferase Assay Kit using a G(5')ppp(5')A RNA cap structure analog as the substrate, while the ExoN activity was evaluated by a FRET-based exoribonuclease assay, for which an RNA duplex substrate with a 20-nucleotide 5' dU overhang was conjugated to a Cy3/BHQ2 pair (Table S1 and Figure S3A, B). Notably, as shown in Figure S3E, F, nsp14 exhibited time-dependent and nsp10 dose-dependent increase in the ExoN activity with the maximum activity being reached at *ca.* 80 min in the presence of 4 mol equiv of nsp10, which was used for all of the ExoN activity assays in the primary screening. We then selected a panel of 24 metal-based compounds together with 10 organic-based potential drug candidates (for comparison) (structures are shown in Figure S4) for primary screening for their

potentials as inhibitors of nsp14 MTase and ExoN activities. As shown in Figure 1, in the presence of 50 mol equiv of metal compounds, the MTase activity of nsp14 was inhibited to varying degrees. Notably, $AgNO_3$ and bismuth porphyrin Bi(THPP) and $Bi(NAC)_3$ inhibited nsp14 MTase activity by ca. 95.38 ± 0.49, 95.58 ± 0.28 and 94.50 ± 0.18%, respectively, followed by metal-porphyrin compounds Cu(TPP) and Fe(TPP) (with ca. 91.05 ± 0.60 and 88.16 ± 0.09% of inhibition). It is noted that ebselen, which potently inhibited the main protease and also effectively ejected Zn from Zn-sites of both PLpro and nsp10 of SARS-CoV-2,[34, 35] showed an over 80% inhibition on MTase activity of nsp14, comparable to that of a bismuth drug, ranitidine bismuth citrate (RBC) (Figure S5). Both have been demonstrated to be potential antiviral drugs against SARS-CoV-2,[13, 34] indicating that nsp14 is a promising target of anti-SARS-CoV-2 drugs.

Similarly, most Bi(III)-based compounds exerted over 90% inhibition of the ExoN activity of nsp14/nsp10 (Figure 1). These samples were then subjected to urea-polyacrylamide gel electrophoresis, and the results further confirmed the observation from FRET-based assay (Figure S6A-D). Among the small organic molecular inhibitors screened, aurintricarboxylic acid, ebselen, and disulfiram exhibited obvious inhibitory effects on the ExoN activity of nsp14/nsp10, comparable to that of RBC (Figure S5).

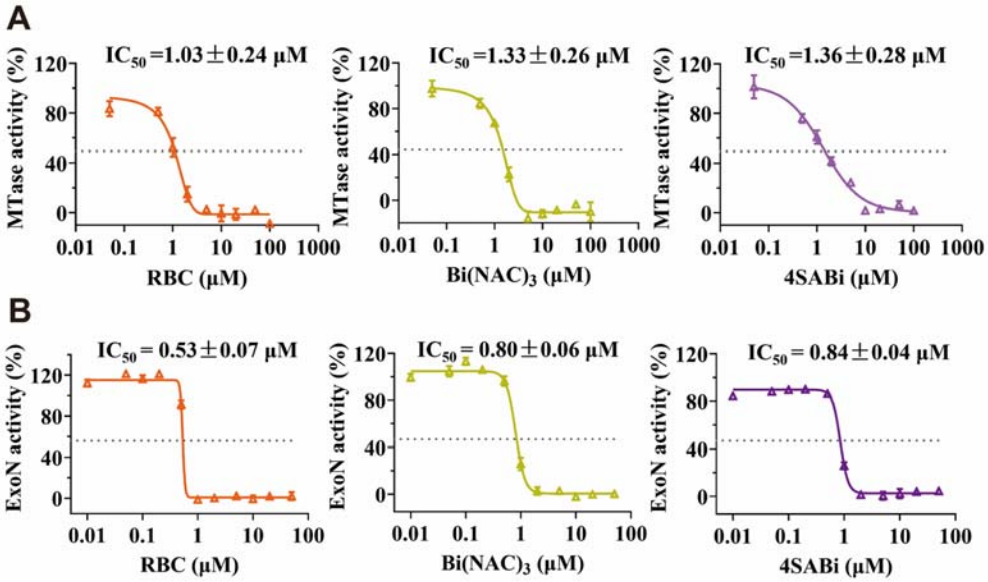

Figure 2. Metal-based compounds as potential inhibitors of nsp14/nsp10. (A) Dose-dependent inhibition of the MTase activity of SARS-CoV-2 nsp14 by RBC, $Bi(NAC)_3$, and 4SABi (n = 3). (B) Dose-dependent inhibition of the SARS-CoV-2

nsp14/nsp10 ExoN activity by RBC, $Bi(NAC)_3$, and 4SABi based on the FRET-based ExoN assay (n = 3). IC_{50} values are presented as mean values ± standard deviation (SD).

We further evaluated the inhibition extent of those compounds that exhibited good inhibitory effect in the primary screening on MTase activity of nsp14 and ExoN activity of nsp14/nsp10 including RBC, $Bi(NAC)_3$, 4SABi, CBS, BABABi, Bi(THPP), Bi(NTA), $AgNO_3$, cisplatin, Zn(TPP) and Fe(TPP). By examining the dose-dependent inhibition of nsp14 activities by these compounds, we determined their half-maximum inhibitory concentration (IC_{50}) for MTase of nsp14 (Figure 2A and Table S2) and ExoN of nsp14/nsp10 (Figure 2B and Table S2). Notably, some metal-based compounds are potent inhibitors of nsp14 in both activities, especially RBC, $Bi(NAC)_3$, and 4SABi, with IC_{50} values of 1.03 ± 0.24, 1.33 ± 0.26, and 1.36 ± 0.28 μM for its MTase activity and 0.53 ± 0.07, 0.80 ± 0.06 and 0.84 ± 0.04 μM for its ExoN activity, respectively, revealing high potentials of these compounds to be developed as anti-SARS-CoV-2 drugs. We also examined the influence of different chelating ligands of Bi(III) on the ExoN activity of nsp14/nsp10 and the MTase activity of nsp14 and found that these ligands showed almost no inhibitory effect on both activity of the enzyme (Figure S7), suggesting that Bi(III) ions may play a critical role in the inhibition of nsp14 enzymatic activities.

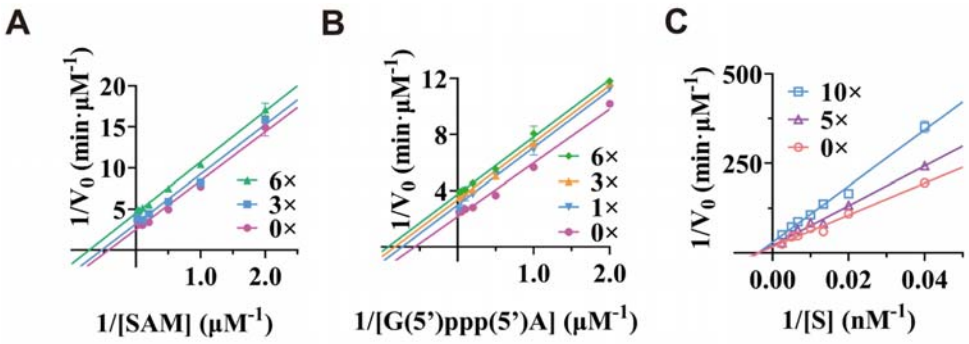

Figure 3. Kinetics analysis of nsp14 activities inhibited by Bi(III) compounds. Lineweaver-Burk plot analysis of kinetics of nsp14 MTase activity inhibited by 4SABi (A, B) and ExoN activity inhibited by RBC (C), respectively (n = 3). Substrates used for MTase activity assays are SAM (A) and the G(5')ppp(5')A RNA analog (B). The apparent Michaelis-Menten constants K_m and V_{max} were calculated and are listed in Tables S3 and S4. Lines of different colors represent the kinetics of the enzyme in the presence of different molar equivalents of Bi(III) compounds.

Given that most Bi(III) compounds showed great inhibitory effects on the methyltransferase activities of nsp14, we next explored their inhibition modes. We selected 4SABi as a showcase to investigate how it inhibited the MTase activity of nsp14. The reaction velocity was plotted against the concentration of two substrates, i.e., SAM and G(5')ppp(5')A RNA analog (Figure 3A, B). The slopes were then used to calculate K_m and V_{max} by nonlinear fitting to the Michaelis-Menten equation (Table S3). For the SAM-dependent kinetic assay, both V_{max} and K_m decreased with the increasing molar equivalences of 4SABi, but the ratio of K_m to V_{max}, which is the slope in the double-reciprocal plot (Figure 3A), kept unchanged. Similar trends were also observed in the G(5')ppp(5')A RNA-dependent kinetic assay (Figure 3B). These results suggest that Bi(III) allosterically inhibits nsp14 methyltransferase activity via an uncompetitive mode.

Similarly, we also explored the influence of Bi(III) compounds on the kinetics of ExoN activity of the nsp14/nsp10 complex using RBC as an example. In the presence of different molar equivalents of RBC, K_m values were maintained at around 300 nM, while V_{max} values decreased obviously as the molar equivalence of RBC increased (Figure 3C and Table S4), suggesting that Bi(III) allosterically inhibits the ExoN activity of nsp14/nsp10 via a noncompetitive mode. We further investigated the effects of RBC on the RNA-binding capability of SARS-CoV-2 nsp14/nsp10 by an electrophoretic mobility shift assay (EMSA). In the absence of metal-based compounds, a significant shift of the dsRNA substrate in the gel indicated the formation of the nsp14-RNA complex. Relative band intensities of the native-PAGE were quantified by ImageJ. Supplementation of gradient amounts of RBC to the mixture of nsp14 and dsRNA showed negligible effects on the formation of the protein-RNA complex (Figure S8), in consistence with the proposed noncompetitive mode of inhibition of nsp14 ExoN activity by the compounds.

Bi(III) Compounds Allosterically Inhibit the Enzymatic Activities of nsp14/nsp10 through Substitution of Its Essential Zn(II). We next explored the mechanism of inhibition of nsp14/nsp10 activity by Bi(III) compounds. Both nsp14 and nsp10 are zinc-finger proteins, with three zinc fingers in nsp14 and two zinc fingers in nsp10. These zinc fingers play significant roles in the functions of the nsp14/nsp10

complex.[36, 37] Considering the high thiophilic nature of Bi(III),[13, 33, 38] we hypothesized that Bi(III) compounds may inhibit nsp14 activity through the coordination of Bi(III) ions to the cysteine residues at the zinc-finger sites.

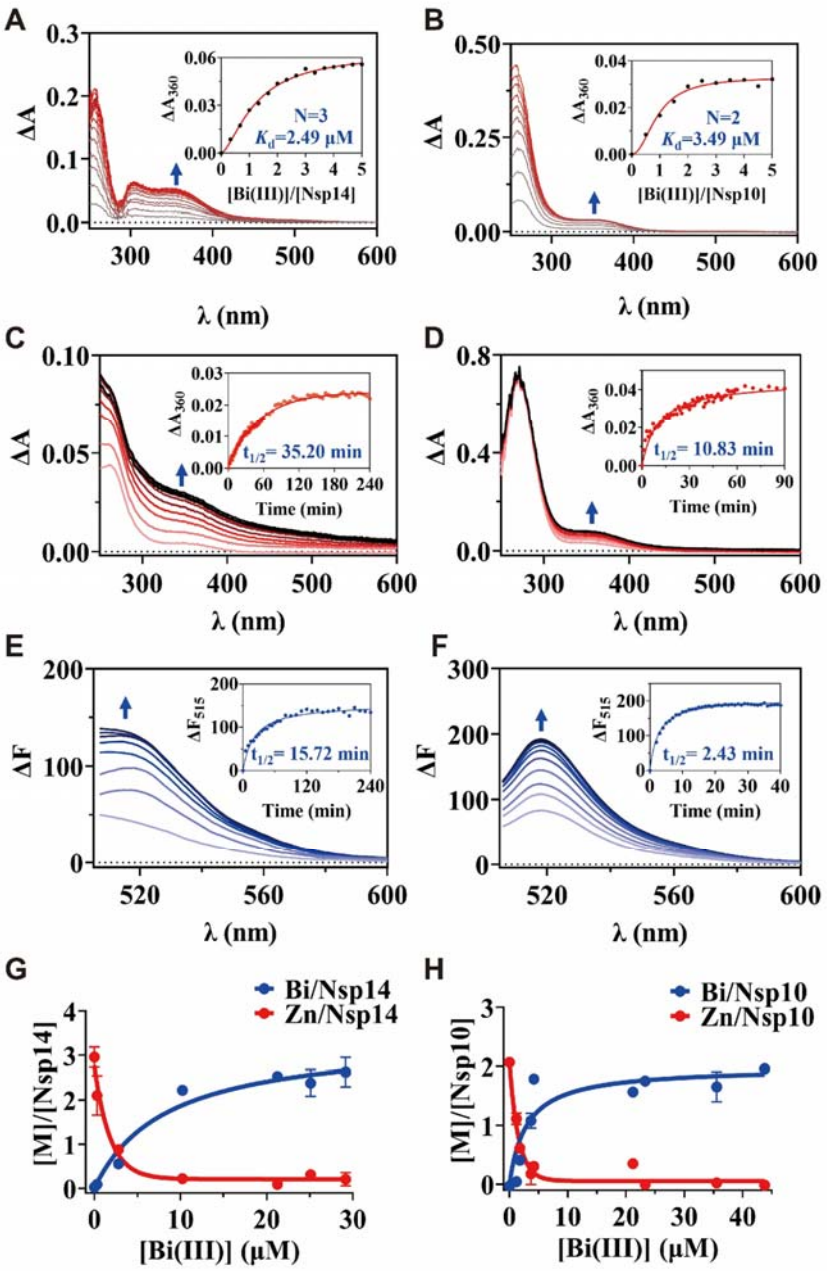

Figure 4. Displacement of essential Zn(II) by Bi(III) in SARS-CoV-2 nsp14 and nsp10 upon Bi(III) treatment. (A, B) UV-vis spectra of apo-nsp10 (A) and apo-nsp14 (B) titrated by Bi(NTA). The absorption at 360 nm was plotted against Bi(III)/protein ratios (inset). (C, D) Time-dependent UV-vis spectra of Bi(III) binding to native nsp14 (C) and nsp10 (D). (E, F) Kinetic analysis of Zn(II) releasing from nsp14 (E) and nsp10 (F) by fluorescence spectroscopy. (G, H) The substitution of Zn(II) in

native nsp14 (G) and nsp10 (H) by CBS using equilibrium dialysis. The metal content was determined by inductively coupled plasma mass spectrometry (ICP-MS) (n = 3).

To validate this, we first examined the binding of Bi(III) (as Bi(NTA)) to both apo-nsp14 and apo-nsp10 by UV-vis spectroscopy. As shown in Figure 4A, B, the addition of Bi(III) led to the appearance and increase in an absorption band at around 360 nm, characteristic of the Bi–S ligand-to-metal charge-transfer (LMCT) band.[39, 40] The absorption band leveled off at the molar ratios of 3:1 and 2:1 for Bi(III)/nsp14 and Bi(III)/nsp10, indicative of three and two Bi(III) bound per nsp14 and nsp10, respectively. The dissociation constants for Bi(NTA) to nsp14 or nsp10 were determined to be 2.49 ± 0.26 μM and 3.49 ± 0.91 μM, respectively, by fitting the data into the Ryan–Weber nonlinear equation. Taking into account the binding constant of Bi(III) ion to NTA (log K=17.55),[41] the dissociation constants for Bi(III) ion to nsp14 or nsp10 were calculated to be $0.70(\pm0.07)\times10^{-17}$ μM and $0.98(\pm0.26)\times10^{-17}$, respectively.

We then investigated whether Bi(III) could also bind to native nsp10 (Zn_2-nsp10) and nsp14 (Zn_3-nsp14), leading to zinc release from the enzymes. We first monitored the binding kinetics by UV–vis spectroscopy upon the incubation of excess amounts (20 mol equiv) of Bi(NTA) with native enzymes. As shown in Figure 4C, D, the appearance and increase of absorption bands at 360 nm indicated the bindings of Bi(III) to Zn_3-nsp14 or Zn_2-nsp10. By fitting the data into a pseudo first-order reaction, we demonstrated that Bi(III) bound to Zn_2-nsp10 much faster than to Zn_3-nsp14 with $t_{1/2}$ of 10.83 ± 0.01 min and 35.20 ± 3.29 min, respectively (Figure 4C, D, inset). We further monitored zinc release by fluorescence spectrometry using a zinc-selective fluorescent dye, FluoZin-3 (Figure 4E, F). Upon the treatment of native enzymes with 20 mol equiv of Bi(NTA), we observed a time-dependent increase in the emission band at 515 nm. By fitting kinetic data into a pseudo-first-order reaction, the time for release of half of Zn(II) ions from the enzymes, $t_{1/2}$, was determined to be 15.72 ± 2.81 min and 2.43 ± 0.17 min for native nsp14 and nsp10 respectively, indicating that the Zn(II) release is faster than Bi(III) binding for both enzymes (Figure 4E, F, inset).

We further investigated the binding of Bi(III) to the native enzymes as well as Zn(II) release, using equilibrium dialysis with the metal contents being determined by inductively coupled plasma mass spectrometry (ICP-MS). As shown in Figure 4G, H, the addition of increasing amounts of Bi(III) (as CBS) to the native nsp10 and nsp14 resulted in *ca.* 1.99 ± 0.11 and 2.60 ± 0.61 mol equiv of Bi(III) bound to nsp10 and nsp14, accompanied by *ca.* 2.08 ± 0.10 and 2.75 ± 0.27 mol equiv of Zn(II) removal from nsp10 and nsp14, respectively. The data were fitted by one-site binding Hill plot, which gave rise to dissociation constants (K_d) of 2.66 ± 0.06 μM and 8.27 ± 0.54 μM and the maximal binding capacity (B_{max}) of 1.99 ± 0.05 and 3.41 ± 0.08 for nsp10 and nsp14, respectively, indicating that 2 and 3 Bi(III) ions bound per nsp10 and nsp14, respectively. Taken together, we demonstrate that Bi(III) compounds could replace Zn(II) ions at the zinc-finger sites of the enzymes with Bi(III) ions, which is accountable for their inhibitory effects on the nsp14/nsp10 activity.

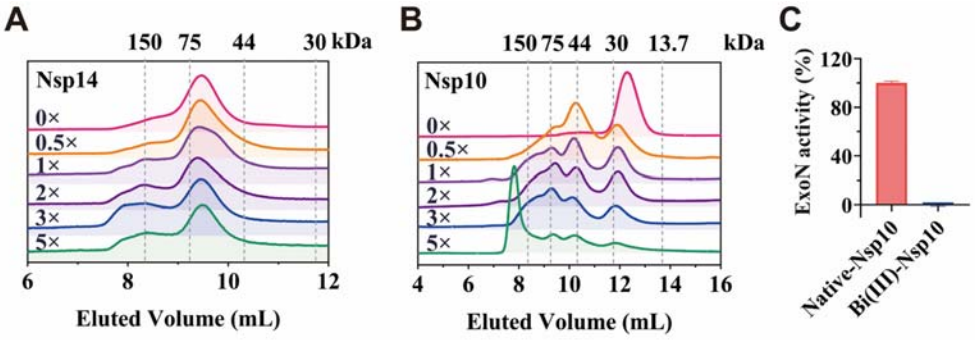

Figure 5. Quaternary structure changes in SARS-CoV-2 nsp14 and nsp10 upon Bi(III) treatment. (A, B) Size-exclusion chromatography profiles of native-nsp14 (A) and native-nsp10 (B) in the presence of increasing molar equivalents of Bi(III). The elution volumes of the standards are indicated based on the calibration using a gel filtration low-molecular-weight (LMW) calibration kit (GE Healthcare). Molecular weights of standards (kDa) are indicated at the top of each figure. (C) Relative ExoN activity of SARS-CoV-2 nsp14 in the presence of Zn-nsp10 and Bi(III)-nsp10 (n = 3).

As nonessential metal ions often lead to protein quaternary structural changes,[38, 40, 42, 43] we next investigated the influence of Bi(III) on the quaternary structure of nsp10 and nsp14 by size-exclusion chromatography. As shown in Figure 5A, in the absence of metal compounds, native nsp10 and nsp14 were eluted at 12.3 and 9.4 mL, corresponding to molecular weights of 15 and 60 kDa respectively, indicating that both native nsp10 and nsp14 are in the monomeric states. Upon the incubation of nsp14 with

increasing molar equivalents (0-5) of Bi(III) (as CBS), we observed the decreased intensities in the monomer peaks and appearance and increase in the peaks at an elution volume of ca. 8.4 mL, corresponding to a molecular weight of 150 kDa, suggesting that excess of Bi(III) resulted in only partial oligomerization of nsp14. However, incubating nsp10 with increasing molar equivalents (0-5) of Bi(III) led to an almost complete disappearance of the nsp10 monomer and a gradual appearance of new peaks at 11.8, 10.3, and 9.3 mL, corresponding to dimer, trimer, pentamer and even larger oligomers, respectively (Figure 5B). In the presence of 5 mol equiv of Bi(III), the majority of nsp10 was eluted at 7.8 mL, corresponding to a molecular weight larger than 150 kDa, indicative of the formation of a higher oligomerization state of nsp10. These results demonstrate that Bi(III) can alter the protein quaternary structures, especially for nsp10.

As the exoribonuclease activity of nsp14 is largely stimulated by nsp10, and nsp10-nsp14 intermolecular interaction involves residues around the zinc finger of nsp10.[36, 37] We then examined the effect of different metal-bound nsp10 on the ExoN activity of nsp14 and found that, in contrast to native Zn(II)-bound nsp10, Bi(III)-bound nsp10 could not stimulate the ExoN activity of nsp14 (Figure 5C), suggesting that the binding of Bi(III) to nsp10 might disrupt its interaction with nsp14, which abrogates the ExoN activity of nsp14.

Bi(III)-Based nsp14/nsp10 Inhibitors Show Antiviral Efficacy in SARS-CoV-2-Infected Mammalian Cells. Based on our enzymatic screening results, we found that metal-based compounds inhibited nsp14/nsp10 activities to different extents. Among the compounds we examined, Bi(III)-based compounds potently inhibited both MTase and ExoN activities of nsp14/nsp10; As(III)-based compound, ZIO-101 and Cu(II)-porphyrin, Cu(TPP) only partially inhibited ExoN and MTase activity of nsp14/nsp10, respectively; while $Ga(NO_3)_3$ and carboplatin showed almost no inhibition on both enzymatic activities. To evaluate the antiviral activity of the metal-based nsp14/nsp10 inhibitors, these compounds with different inhibitory effects on nsp14/nsp10 activity were selected for further antiviral studies in SARS-CoV-2-infected mammalian cells. The 50% cytotoxicity concentrations (CC_{50}) of these compounds were calculated to be >200 μM for 4SABi, 26.46 ± 0.11 μM for ZIO-101, 306.1 ± 5.62 μM for Cu(TPP), >1000 μM

for $Ga(NO_3)_3$, and >500 μM for carboplatin (Figure S9). The compounds at a nontoxic concentration were used to examine their ability to inhibit SARS-CoV-2 BA.5.2 strain replication. As shown in Figure 6A, among the compounds tested, 4SABi, a Bi(III)-based superstructured porphyrin,[44] exhibited the most potent anti-SARS-CoV-2 activity, as evidenced by ~2-log viral load reduction in the VeroE6-TMPRSS2 cell culture supernatant, while other metal-based compounds showed no such obvious inhibition. To further evaluate antiviral potency, the half-maximal effective doses (EC_{50}) were determined to be 0.58 ± 0.01 μM for 4SABi (Figure 6B) against SARS-CoV-2 BA 5.2 strain through microneutralization assays.[45] Considering the rapid mutation of SARS-CoV-2, we also evaluated the antiviral potential of 4SABi against the latest variant of the XBB strain. The results show that the treatment of VeroE6-TMPRSS2 cells infected by SARS-CoV-2 BA 5.2 and XBB strains with gradient amounts of 4SABi reduced viral RNA loads in a dose-dependent manner, as evidenced by the maximal 4-5-log viral load reduction in the cell culture supernatant (Figure 6C, D), indicative of 4SABi as a potential broad-spectrum anti-SARS-CoV-2 agent.

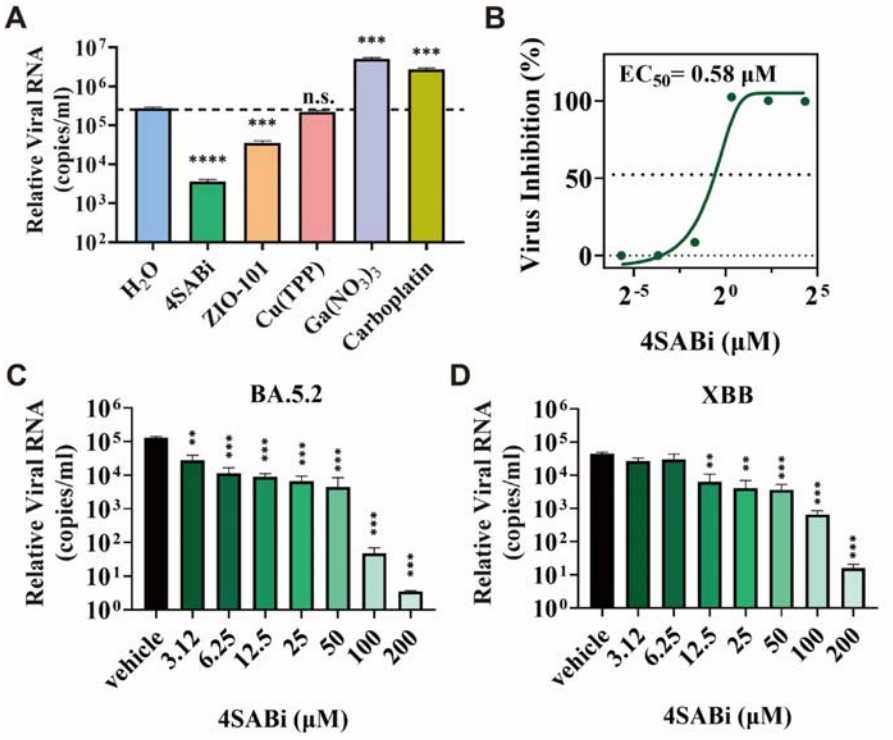

Figure 6. Antiviral efficacy of metal-based nsp14/nsp10 inhibitors. (A) VeroE6-TMPRSS2 cells were infected with SARS-CoV-2 BA.5.2 [multiplicity of infection (MOI) = 0.01] and treated with different metallodrugs for 48 h, and the culture supernatant was then collected for viral load quantitation by quantitative reverse transcription-polymerase chain reaction (qRT-PCR)

(n = 3). The concentrations are 100 μM for 4SABi, 20 μM for ZIO-101, and 200 μM for Cu(TPP), $Ga(NO_3)_3$, and carboplatin. (B) Microneutralization assay of SARS-CoV-2 BA.5.2 strain-infected VeroE6-TMPRSS2 cells (MOI = 0.1) in the presence of 4SABi at the concentration indicated for 24 h (n = 3). Relative percentages of virus inhibition were calculated compared with the vehicle control (0 μM). EC_{50} values are presented as mean values ± SD. (C, D) 4SABi suppressed SARS-CoV-2 BA 5.2 strain (C) and SARS-CoV-2 XBB (D) replication in VeroE6-TMPRSS2 cells (MOI) = 0.01) in a dose-dependent manner. Viral load in the cell culture supernatant was quantified at 48 h postinfection by qRT-PCR. Statistical significance between the drug treatment group and the vehicle group (0 μM) was determined by an unpaired two-tailed Student's *t* test (n = 3); **P < 0.01, ***P < 0.001 and ****P < 0.0001.

Nsp14 is Identified as an Authentic Target of Bi(III) Antivirals in SARS-CoV-2-Infected Mammalian Cells. To further validate whether nsp14 serves as an authentic target of Bi(III) antivirals, we examined whether Bi(III) binds to nsp14 protein in SARS-CoV-2-infected mammalian cells by using our previously developed metal-coding assisted protein quantification method with slight modification (Figure 7A).[46] Briefly, the nsp14 protein from virus-infected cell lysates was enriched and immunoprecipitated with magnetic beads modified with nsp14-specific capture antibodies. Subsequently, the captured nsp14 protein was magnetically separated and interacted with lanthanide (^{155}Gd)-conjugated detection antibodies. The ^{155}Gd-labeled nsp14 detector antibody along with nsp14 was then eluted to the supernatant under acidic conditions. The ^{155}Gd and ^{209}Bi intensities were then monitored simultaneously by ICP-MS to quantify the nsp14 protein and the corresponding content of bound Bi. ^{115}Indium (5 ppb) was used as an internal standard throughout the ICP-MS measurement. As shown in Figure 7B, a similar level of nsp14 could be detected from the virus-infected cell lysates treated without or with a Bi(III) compound (as $Bi(NAC)_3$) judged by the comparable signals of ^{155}Gd/^{115}In. In contrast, no nsp14 could be detected from noninfected cell lysates. Importantly, as shown in Figure 7C, significantly higher bismuth signals could be detected only from the nsp14 extracted from the lysates of virus-infected cells treated with Bi(III); while almost no observable Bi(III) could be found in either the noninfected cell lysates or the lysates of cells without the treatment of Bi(III). Meanwhile, we also determined the Zn(II) content of extracted nsp14 and found that *ca.* 73.0 ± 34.9% of Zn(II) was released from nsp14 after Bi(III) treatment, suggesting that Bi(III)

binds to nsp14, resulting in the displacement of Zn(II) from nsp14 (Figure 7D). This study clearly indicates that nsp14 is an authentic target of Bi(III) not only *in vitro* but also in SARS-CoV-2-infected mammalian cells.

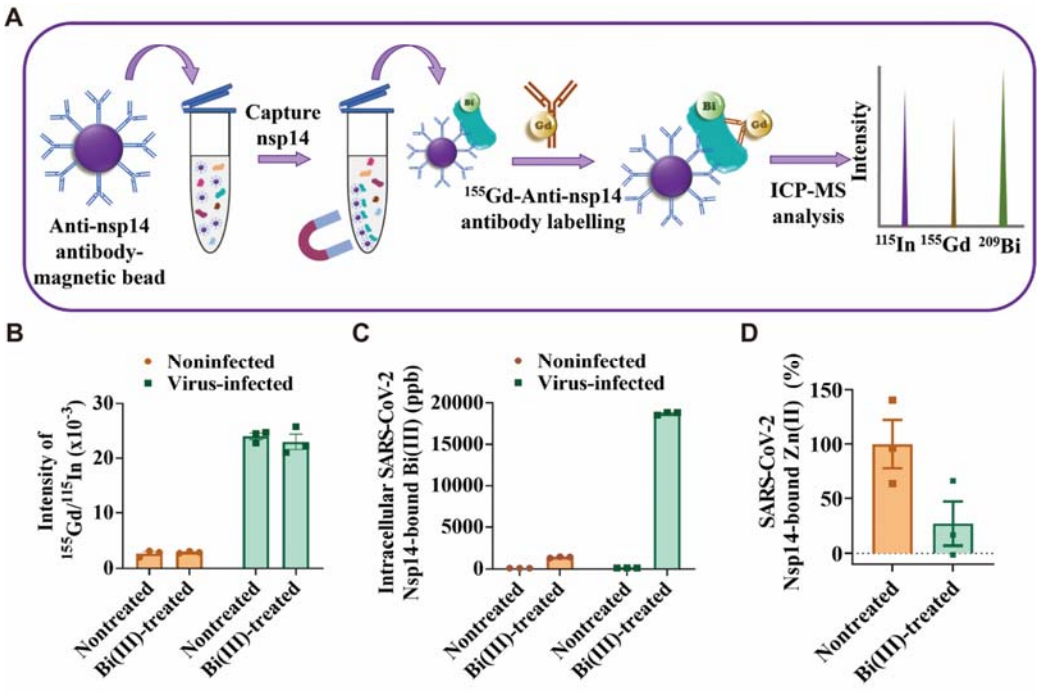

Figure 7. Target validation of nsp14 in mammalian cells. (A) Schematic chart of the target validation of Bi(III) in SARS-CoV-2-infected cells. (B-D) ICP-MS analysis of the relative intensity of $^{155}Gd/^{115}In$ (B) and cellular SARS-CoV-2 nsp14-bound Bi(III) content (C) and nsp14-bound Zn(II) content (D) in SARS-CoV-2-infected VeroE6-TMPRSS2 cells (MOI = 0.1) with or without Bi(III) treatment at 24 h postinfection (n = 3).

Conclusions

In summary, we demonstrate that Bi(III)-based compounds allosterically inhibited both ExoN and MTase activities of SARS-CoV-2 nsp14/10, attributable to their ability to displace the Zn(II) ions from the zinc-finger sites of the enzymes by Bi(III) ions. The binding of Bi(III) to nsp10 and nsp14 also altered the quaternary structures of the enzymes. The broad-spectrum antiviral activity of Bi(III)-based nsp14/nsp10 inhibitors was also validated in mammalian cells infected with different variants of SARS-CoV-2. Significantly, for the first time, we validated nsp14 as an authentic target of Bi(III)-based antivirals

in SARS-CoV-2-infected mammalian cells. Our studies highlight the potential of nsp14/10 as an important target for the development of pan-anti-SARS-CoV-2 agents.

Materials and Methods

Chemicals. Colloidal bismuth citrate (CBS) and ranitidine bismuth citrate (RBC) were kindly provided by the Livzon Pharmaceutical Group. The RBC used in the current study has the composition ranitidine/Bi(III)/citrate = 1:1:1 with the molecular formula $C_{19}H_{27}O_{10}SBi$.[47] $Bi(NAC)_3$ was freshly prepared by mixing CBS with 3 mol equiv of *N*-acetyl-L-cysteine (NAC). Bi(TPP) and Bi(THPP) were prepared as previously described.[48] 4SABi, BABABi, and MAMABi were prepared and characterized according to previous reports.[44, 49, 50] Partial porphyrin compounds were purchased from Shanghai Chemson Chemicals Co, Ltd (China). All other chemicals were purchased from MedChemExpress (MCE) unless otherwise stated.

Cloning, Protein Expression, and Purification. Full-length nsp10 and nsp14 as well as nsp14 MTase and ExoN domain of SARS-CoV-2 isolate Wuhan-Hu-1, complete genome (NCBI GenBank accession no. NC_045512.2) were cloned into pET-28-a(+) with an N-terminal 6× His-tag, generating pET28a-nsp10 and pET28a-nsp14 respectively. pET28a-nsp10 and pET28a-nsp14 were transformed into *Escherichia coli* DH10B before sequencing validation. Validated plasmids of pET28-nsp10 and pET28a-nsp14 were then transformed into Rosetta (DE3) pLysS. Cells harboring pET28a-nsp10 and pET28a-nsp14 were cultured in 2x YT medium overnight at 37 °C with a supplementation of 50 μg/ml kanamycin and 20 μg/ml chloramphenicol. The cells were then amplified with 1:100 dilutions in 2x YT medium at 37 °C, and the expression of nsp10 and nsp14 was induced by adding 0.05 mM (for nsp10) and 0.3 mM (for nsp14) isopropyl *β*-D-thiogalactoside (IPTG) when OD_{600} reached 0.7. After induction at 16 °C for 18 h with agitation at 160 rpm, cells were harvested by centrifugation at 5000*g*, 4 °C for 30 min, washed twice with phosphate-buffered saline (PBS), and then resuspended and lysed by sonication in PBS supplemented with 5 mM b-mercaptoethanol (only for nsp10), 0.1% Triton X-100, 1 mM phenylmethylsulfonyl fluoride (PMSF), 40 mM imidazole, and 10 mg/L DNase I. Recombinant nsp10 and nsp14 were

centrifuged at 15,000*g*, 4 °C for 45 min, and then purified by a Ni-NTA column (Thermo Fisher Scientific) washed with Tris-NaCl buffer (50 mM Tris-HCl, pH 7.5, 300 mM NaCl, 5 mM $MgSO_4$) containing a gradient imidazole. The His tags of nsp10 and nsp14 were removed by Thrombin Protease. Nsp10 was further purified using a Superdex 200 Increase 10/300 GL column (GE Life Sciences) eluted with gel filtration buffer (20 mM HEPES, pH 7.4, 150 mM NaCl, 5 mM $MgCl_2$, and 5% glycerol). Full-length Nsp14 was further purified by HiTrap S ion-exchange chromatography (GE Healthcare). All purified proteins were checked by SDS-PAGE, and the identity of nsp10 and nsp14 was confirmed by LC-MS after trypsin digestion. Proteins were then aliquoted and stored at -80 °C in HEPES buffer (20 mM HEPES, pH 7.4, 150 mM NaCl, 5 mM $MgCl_2$ and 5% glycerol) for further use.

Methyltransferase (MTase) Activity Assay. An MTase-Glo Methyltransferase Assay Kit (Promega) was used to measure the MTase activity, and a G(5')ppp(5')A RNA Cap Structure Analog (New England Biolabs) was used as the substrate for the assay. Progression of the reactions was monitored by luminescence in white 384-well plates (Corning) by using a SpectraMax iD3 multimode microplate reader.

To determine the IC_{50} value of drugs toward the inhibition of the MTase activity of nsp14, 10 μM nsp14 was preincubated with equal volumes of drugs at 0, 0.5, 5, 10, 20, 50, 100, 200, 500, and 1000 μM for 2 h on ice before the methyltransferase reaction. 16 μL MTase reactions (final concentration of 1 μM for nsp14 incubated with a serial dilution of drugs, 20 μM for SAM and 20 μM for G(5')ppp(5')A RNA Cap Structure Analog, respectively) were carried out in MTase reaction buffer (20 mM Tris-HCl, pH 8.0, 50 mM NaCl, 3 mM $MgCl_2$, 0.1 mg/mL BSA, 0.5 mM TCEP) and were incubated for 30 min at room temperature. Then, 4 μL of 5x Methyltransferase-Glo Reagent was added, mixed well, and incubated at room temperature for 30 min. After that, 20 μL of Methyltransferase-Glo Detection Solution was added and mixed well, followed by incubation for another 30 min at room temperature. Luminescence was then recorded by the microplate reader, and dose-dependent curves for the IC_{50} value were determined by nonlinear regression using GraphPad Prism.

For the MTase kinetic assays, an SAH standard curve was first prepared to assess linearity of the assay and to calculate the amount of the reaction product SAH produced in each reaction. 8 μL of MTase

reaction buffer containing serial diluted SAH (from 0 to 1 μM) was incubated with 2 μL of 5x Methyltransferase-Glo Reagent for 30 min at room temperature followed by the addition of 10 μL of detection solution as described above. Luminescence was recorded and then plotted against the SAH concentration by linear regression using GraphPad Prism. Before the methyltransferase reaction, nsp14 (20 μM) was incubated with an equal volume of drugs at the specified molar ratio for 2 h on ice. MTase kinetic assays were carried out in 8 μL of MTase reaction buffer containing nsp14 (1 μM) incubated with drugs, 2 μL of 5x Methyltransferase-Glo Reagent, together with 25 μM G(5')ppp(5')A RNA Cap Structure Analog and serially diluted SAM (0, 0.5, 1, 2, 5, 10, 20, and 50 μM) for SAM-dependent kinetic assays, or 25 μM SAM and serially diluted G(5')ppp(5')A RNA Cap Structure Analog (0, 0.5, 1, 2, 5, 10, 20, and 50 μM) for G(5')ppp(5')A RNA-dependent kinetic assays at room temperature for 10 min, followed by adding 2 μL of 0.5% trifluoroacetic acid (TFA) to stop the reaction. After that, 10 μL of Methyltransferase-Glo Detection Solution was added and mixed well, followed by incubation for another 30 min at room temperature. The control group was tested in the absence of drugs under the same condition. The amounts of SAH produced in different intervals were calculated by a standard curve to determine the velocity of the reaction. The velocity was plotted against the concentration of the substrates. Slopes were then used to calculate the K_m and V_{max} by nonlinear fitting to the Michaelis-Menten equation using GraphPad Prism.

FRET-Based Exoribonuclease (ExoN) Activity Assay. A slightly modified double-stranded RNA with a 20-nucleotide 5' dU overhang, conjugated to a Cy3-quencher (BHQ2) pair, was used as the substrate for the exoribonuclease activity assay based on a previous report.[51] Nsp14 and nsp10 were mixed in a molar ratio of 1:4 to form the nsp14/nsp10 complex. Progression of the reactions was monitored by fluorescence (λ_{ex} = 545 nm, λ_{em} = 585 nm) in black 96-well plates (Thermo Fisher Scientific) using a SpectraMax iD3 multimode microplate reader. ExoN activities were calculated by the amount of fluorescence released after the initial reading.

For the inhibitor screening, 10 μM of nsp14/nsp10 complex was preincubated with an equal volume of 500 μM drugs on ice for 2 h. After the mixture was added to achieve the final concentration of 200 nM (nsp14/nsp10 complex) and 10 μM (inhibitors), the reaction (100 μL) was carried out at 25 °C for 3 h in

the ExoN reaction buffer (50 mM Tris-HCl, pH 8.0, 30 mM NaCl, 2.5 mM $MgCl_2$, 10 mM K_2HPO_4, 0.5 mM tris(2-carboxyethylphosphine (TCEP) and 0.1 mg/mL BSA) containing 200 nM Cy3/quencher-dsRNA substrates. The fluorescence signal was monitored in real time by a SpectraMax iD3 multimode microplate reader. Reactions were then analyzed by 19.5% 7 M of urea-containing denaturing polyacrylamide gel electrophoresis (30% solution of 37.5:1 acrylamide: bis-acrylamide, BioRad) in TBE (Tris-borate EDTA) buffer. Electrophoresis was carried out at 250 V for 40 min. Gels were subsequently stained with GelRed (Sigma-Aldrich) for 5 min at room temperature. The stained gels were visualized through the iBright CL750 Imaging System (Thermo Fisher Scientific).

For determination of the half-maximum inhibitory concentration (IC_{50}), nsp14/nsp10 complex (10 μM) was preincubated with an equal volume of drugs (0, 2, 10, 20, 40, 100, 200, 400, 1000, 2000, 4000, and 10,000 μM) for 2 h on ice before the nuclease reaction. Nuclease assays (100 μL) were performed at 25 °C for 1 h in ExoN reaction buffer in the presence of 50 nM Cy3/quencher-dsRNA substrates and 50 nM nsp14/nsp10 complex incubated with drugs. Dose-response curves for the IC_{50} value were determined by nonlinear regression using GraphPad Prism.

For the ExoN kinetic assays, nsp14/nsp10 complex (10 μM) was incubated with an equal volume of drugs at the specified molar ratio for 2 h on ice before the nuclease reaction. Nuclease kinetic assays were carried out in 100 μL of ExoN reaction buffer containing 100 nM (for RBC) nsp14/nsp10 complex incubated with drugs and serially diluted Cy3/quencher-dsRNA substrates (0, 25, 50, 75, 100, 150, 200, 300, 400, and 500 nM). The control group was performed in the absence of drugs under the same condition. The maximum of the first derivative over the first hour was calculated to determine the velocity of the reaction. The velocity was plotted against the concentration of the substrates. Slopes were then used to calculate the K_m and V_{max} by nonlinear fitting to the Michaelis-Menten equation using GraphPad Prism.

Electrophoretic Mobility Shift Assays (EMSAs). RNA-binding capability of nsp14 was determined by EMSA. For the protein dose-dependent RNA-binding assays, 200 nM of the ExoN substrate dsRNA was incubated with varying concentrations of SARS-CoV-2 nsp14 (0, 0.4, 0.8, 1.2, 1.6, 2.0, 4.0, and 8.0 μM) in HEPES buffer at room temperature for 15 min. For the bismuth(III) addition assays, nsp14

(4 μM) was preincubated with various concentrations of drugs (0, 1, 2, 4, 8, 20, 40 μM) in HEPES buffer for 2 h on ice before the RNA-binding assays before incubating with 200 nM of dsRNA at room temperature for 15 min. Approximately 20 μL of the reaction mixture was then loaded onto 6% native-polyacrylamide gels and electrophoresed in 1xTBE buffer. Electrophoresis was carried out at 100 V for 50 min. Gels were subsequently stained by GelRed (Sigma Aldrich) for 5 min at room temperature and visualized through the iBright CL750 Imaging System (Thermo Fisher Scientific).

UV-Vis Spectroscopy. UV-vis spectra were recorded on a Varian Cary 60 spectrophotometer at room temperature. Binding kinetics of Bi(III) to SARS-CoV-2 nsp10 and nsp14 were determined by incubating Zn_3-nsp14 (2.5 μM) and Zn_2-nsp10 (20 μM) and with 20 mol equiv of Bi-NTA in HEPES buffer. Spectra were then recorded between 200 and 800 nm in a 0.1 cm quartz cuvette every minute. The UV absorption at 360 nm was plotted against time and the curves were then fitted to the binding kinetics equation using GraphPad Prism to calculate the first-order rate constant (k) and the half-life ($t_{1/2}$).

UV-vis titrations of Bi(III) to apo-SARS-CoV-2 nsp10 and nsp14 were carried out at room temperature on a Varian Cary 50 spectrophotometer. Apo-nsp10 (30 μM) and apo-nsp14(7.5 μM) were prepared by dialysis in zinc(II) chelating buffer (20 mM HEPES, pH 7.4, 150 mM NaCl, 5 mM $MgCl_2$, 5% glycerol, 1.5 mM EDTA, 0.5 mM TCEP) supplemented with 50 mol equiv of EDTA at 4°C overnight, followed by the removal of EDTA by dialysis in HEPES buffer. Aliquots of 3 mM Bi-NTA were stepwise added to 200 μL of 30 μM apo-nsp10 or 7.5 μM apo-nsp14 in HEPES buffer. The absorption at 360 nm was plotted against the Bi(III)/protein ratio. The ultraviolet titration curves were fitted into a Ryan-Weber nonlinear equation to determine the dissociation constant (K_d).[40]

Zinc(II) Displacement Analysis. Zinc(II) displacement from nsp10 and nsp14 was determined by inductively coupled plasma mass spectrometry (ICP-MS) (Agilent, 7700x). SARS-CoV-2 nsp14 or nsp10 was incubated with 3 mol equiv of $ZnSO_4$ in dialysis buffer (20 mM HEPES, pH 7.4, 150 mM NaCl, 5 mM $MgCl_2$, 5% glycerol, 0.5 mM TCEP) with mild shaking at 4 °C overnight, followed by the removal of unbound zinc(II) ions in Zn-free dialysis buffer to make the fully Zn-bound proteins. Dialysis tubes loaded with 100 μL of Zn-bound proteins (5 μM for nsp14 and 20 μM for nsp10) or protein buffer were

placed into 50 mL of dialysis buffer in the presence of different concentrations of bismuth(III) compounds with mild shaking at 18 °C overnight. The protein concentration was measured by a bicinchoninic acid (BCA) assay (Thermal Fisher Scientific), and the metal concentration of solution both inside and outside the dialysis tubes was determined by ICP-MS. The maximal binding capacities (B_{max}) and dissociation constants (K_d) were obtained by nonlinear fitting to a one-site binding equation: $Y = B_{max} \times X/(K_d + X)$ using GraphPad Prism 8.

FluoZin-3 (Thermo Fisher Scientific) was used to determine the released-zinc(II) from the protein. Briefly, 1 μM Zn-nsp14 or 1 μM Zn-nsp10 was incubated with 20 mol equiv of Bi-NTA and 5 μM FluoZin-3 in HEPES buffer. Fluorescence kinetics spectra were then recorded between 500 and 600 nm in a 1 cm quartz cuvette every minute on a Hitachi F-7000 fluorescence spectrophotometer at room temperature. The fluorescence emission at 515 nm was plotted against time, and the curves were then fitted to the binding kinetics equation using GraphPad Prism to calculate the half-life ($t_{1/2}$).

Size-Exclusion Chromatography Analysis. Size-exclusion chromatography was performed with a Superdex 75 increase 100/200 GL analytical column (Cytiva) at 4°C. The column was pre-equilibrated by PBS buffer. Nsp10 (20 μM) or nsp14 (5 μM) were preincubated with different molar equivalents of CBS for 1 h at 4 °C. Samples were prepared in PBS buffer to a final volume of 500 μL before loading to the column at a flow rate of 0.8 mL/min.

Cytotoxicity Assay. Cell viability was measured 24 h after incubation of VeroE6 cells with compounds by using the cell proliferation assay kit II (XTT) (Roche), according to the manufacturer's recommendations.

Cellular Antiviral Activity Assay. A viral load reduction assay was performed for the evaluation of cellular antiviral activity, as described previously but with modifications.[52, 53] Briefly, SARS-CoV-2-infected (MOI = 0.01) VeroE6-TMPRSS2 cells were treated with different concentrations of metallodrugs. The culture supernatants of the infected cell were harvested at 48 h postinfection (hpi) for analysis of viral replication. 100 μL of culture supernatant was lysed with 50 μL of RLT buffer and subsequently extracted

for total RNA with the QIAamp viral RNA mini kit (Qiagen). Quantitative reverse transcription-polymerase chain reaction (qRT-PCR) was used for quantitation of SARS-CoV-2 viral load using the One Step TB Green PrimeScript RT-PCR Kit II (Takara) with a LightCycler 480 Real-Time PCR System (Roche). The primers and probe sequences were against the RNA-dependent RNA polymerase/Helicase (RdRp/Hel) gene region of SARS-CoV-2: forward primer: 5'CGCATACAGTCTTRCAGGCT-3'; reverse primer: 5'-GTGTGATGTTGAWATGACATGGTC-3'; specific probe: 5'-FAMTTAAGATGTGGTGCTTGCATACGTAGAC-IABkFQ-3'.

Live Virus Microneutralization assay. Live virus microneutralization assay was performed for the determination of a 50% antiviral effective dose (EC_{50}), as described previously but with slight modification.[45] SARS-CoV-2 was mixed with serially diluted test compounds in 96-well plates and incubated for 1 h at 37 °C in 5% CO_2. The virus-compound mixtures (MOI = 0.1) were then transferred to preseeded VeroE6-TMPRSS2 cells. After further incubation for 24 h, the culture medium was removed, and the plates were airdried. Then, cells were fixed, permeabilized, and incubated with rabbit antiserum raised in-house against the SARS-CoV-2 N protein for 1 h at room temperature, followed by incubation with an Alexa Fluor 488-conjugated goat anti-rabbit IgG (H+L) cross-adsorbed secondary antibody (Life Technologies). SARS-CoV-2 foci were quantitated using Sapphire Biomolecular Imager (Azure Biosystems), and images were analyzed using the ImageJ software. The percentages of neutralization inhibition relative to the control (*i.e.,* without the addition of the compound) wells were determined for each compound concentration. EC_{50} values were calculated by nonlinear regression using GraphPad Prism.

Magnetic Beads Functionalization with Capture Antibodies. To conjugate nsp14 capture antibodies (Sigma) on magnetic beads, N-hydroxysuccinimide (NHS) activated magnetic beads were used to covalently immobilize proteins through the reaction with primary amines of proteins. After the preservation buffer was removed using a magnetic stand, the NHS-activated magnetic beads were activated in ice-cold hydrochloric acid (1 mM, pH 3.0). The antibodies (50 μg) that remained to be labeled were added into the magnetic beads (4 mg) immediately after the removal of hydrochloric acid. The mixture of the antibodies and magnetic beads was incubated for 2 h at room temperature on a rotator. A glycine solution

(0.1 M, pH 2.0) was added after incubation, and the antibody labeled magnetic beads were washed with ultrapure water twice followed by quenching the reaction in ethanolamine (3 M, pH 9.0). The magnetic beads were then washed with ultrapure water and PBS twice and then preserved in PBS buffer.

Nsp14 Antibody Conjugation with Metal-Tags. Nsp14 protein-specific detector antibodies (ProSci) were labeled with ^{155}Gd using the MaxPAR antibody conjugation kits according to the company's recommended protocol.

Evaluation of the Binding of Bi with nsp14 Proteins by ICP-MS. For cell lysate preparation, SARS-CoV-2 (BA.5.2 strain)-infected (MOI = 0.1) and noninfected VeroE6-TMPRSS2 cells were treated with or without 1500 μM of $Bi(NAC)_3$ for 24 h. The culture medium was removed, and the cells were harvested in 1 mL of 1% Triton-100X, which was diluted in PBS to a total protein concentration of around 2 mg/mL. We have previously established a method for protein quantification based on ICP-MS by introducing metal-tagged antibodies.[46] Herein, we used a similar approach to evaluate the binding of Bi to nsp14 proteins. Generally, the magnetic beads functionalized with the capture antibodies specific to nsp14 proteins were blocked in a blocking buffer (PBS, 0.1% Tween-20, and 2.5% BSA) for 30 min at room temperature. The cell lysates were diluted (1:5) using assay buffer (PBS contained 2.5% BSA, 0.1% Tween-20, 0.3% Triton-100), and 100 μL of diluted samples was incubated with functionalized magnetic beads for 30 min at room temperature. The magnetic beads were then washed with washing buffer (PBS, 0.1% Tween-20) three times followed by incubation with ^{155}Gd-labeled nsp14 detection antibodies for 30 min at room temperature. The magnetic beads were then washed with PBS four times and 100 μL of elution buffer (1% HNO_3) was added into each tube to release the metal-tagged antibodies and captured nsp14 proteins. The magnetic stand was used throughout the experiment during washing and elution step to separate magnetic beads from reaction solution. The released solution was diluted in 300 μL of 1% HNO_3 with 5 ppb indium (In) as an internal standard for ^{155}Gd and ^{209}Bi quantification by ICP-MS.

Statistical Analysis. All statistical analyses were performed on three independent experiments, or more if otherwise stated, using Prism 8.0 (GraphPad Software Inc.) software.

Supporting Information

The Supporting Information is available free of charge at https://pubs.acs.org/doi/10.1021/acsinfecdis.3c00356

Sequence alignment of coronaviruses nsp14, SARS-CoV-2 nsp10 and nsp14 expression and purification, MTase-Glo^{TM} methyltransferase assay and FRET-based exoribonuclease assay for purified nsp14, chemical structures of selected compounds, inhibition of nsp14/nsp10 activity by small organic molecular compounds, Urea-PAGE of primary nsp14/nsp10 exoribonuclease inhibitors screening, influence of different ligands on nsp14 activity, influence of RBC on the binding of SARS-CoV-2 nsp14 to ExoN substrates, cytotoxicity of SARS-CoV-2 nsp14 inhibitors against Vero E6 cells, substrate oligonucleotides, IC_{50} of the selected compounds against nsp14/nsp10 activity, K_m and V_{max} values of nsp14/nsp10 activity upon Bi(III) treatment (PDF)

Author Contributions

J.C., H.L., S.Y., and H.S. designed the experiments. B.B. designed the superstructured bismuth porphyrins, J.C. purified the proteins and prepared the compounds. J.C., and X.X. performed all of the *in vitro* enzyme-based assays. Z.Q., C.O., X.W., and Z.-W.Y. performed the antiviral evaluation in cell culture and provided the virus-infected cell lysate. Y.Z., J.C. and X.W. performed the cellular antiviral target validation and analysed the data. J.C. and H.L. wrote the manuscript with input from Y.Z. H.S., S.Y., J.F.-W.C., and D.J. provided conceptual advice and troubleshooting. H.S. supervised the study.

Acknowledgments

This work was partly supported by funding to The University of Hong Kong: the Research Grants Council (17318322, T11-709/21-N, SRFS2122-7S04, C7034-20E, C7142-20G, 17308921, and N_HKU767/22), Health and Medical Research Fund (20190732, 21200562), the Food and Health Bureau; Innovation and

Technology Commission (Health@InnoHK, ITS278/20), the Government of the Hong Kong Special Administrative Region; Guangzhou Laboratory (EKPG22-01); the National Key Research and Development Program of China (2021YFC0866100); and the University of Hong Kong (URC and Norman & Cecilia Yip Foundation).

Abbreviations

nsp, nonstructural protein; ExoN, exoribonuclease; MTase, methyltransferase; RBC, ranitidine bismuth citrate; CBS, colloidal bismuth subcitrate; NAC, *N*-acetyl-L-cysteine; ORF, open reading frame; EMSA, electrophoretic mobility shift assay; LMCT, ligand-to-metal charge transfer; K_d, dissociation constants; B_{max}, maximal binding capacity; CC_{50}, 50% cytotoxicity concentration.

References

(1) WHO Coronavirus Disease (COVID-19) Situation Report, 2023. https://covid19.who.int.

(2) Zhou, Y.; Ip, T. K.-Y.; Zhang, Q.; Li, H.; Sun, H. Metal Complexes as Drugs and Therapeutic Agents. In *Comprehensive Coordination Chemistry III*; Constable, E. C.; Parkin, G.; Que Jr, L., Eds.; Elsevier, 2021; Chapter 9.20, pp 680-705.

(3) *Biological Chemistry of Arsenic, Antimony and Bismuth*; Sun, H., Ed.; John Wiley & Sons, Incorporated, 2011.

(4) Farrell, N. P. Multi-platinum anti-cancer agents. Substitution-inert compounds for tumor selectivity and new targets. *Chem. Soc. Rev.* **2015**, *44* (24), 8773-8785 10.1039/C5CS00201J.

(5) Griffith, D. M.; Li, H.; Werrett, M. V.; Andrews, P. C.; Sun, H. Medicinal chemistry and biomedical applications of bismuth-based compounds and nanoparticles. *Chem. Soc. Rev.* **2021**, *50* (21), 12037-12069 10.1039/D0CS00031K.

(6) Wang, R.; Li, H.; Ip, T. K.-Y.; Sun, H. Bismuth Drugs as Antimicrobial Agents. In *Advances in Inorganic Chemistry;* Sadler, P. J.; van Eldik, R., Eds.; Academic Press, 2020; Chapter 6, Vol. 75, pp 183-205.

(7) Li, H.; Wang, R.; Sun, H. Systems approaches for unveiling the mechanism of action of bismuth drugs: New medicinal applications beyond *Helicobacter pylori* infection. *Acc. Chem. Res.* **2019**, *52* (1), 216-227 10.1021/acs.accounts.8b00439.

(8) Berners-Price, S. J.; Filipovska, A. Gold compounds as therapeutic agents for human diseases. *Metallomics* **2011**, *3* (9), 863-873 10.1039/c1mt00062d.

(9) Frei, A.; Verderosa, A. D.; Elliott, A. G.; Zuegg, J.; Blaskovich, M. A. T. Metals to combat antimicrobial resistance. *Nat. Rev. Chem.* **2023**, *7* (3), 202-224 10.1038/s41570−023−00463−4.

(10) Zhang, Q.; Wang, R.; Wang, M.; Liu, C.; Koohi-Moghadam, M.; Wang, H.; Ho, P. L.; Li, H.; Sun, H. Re-sensitization of mcr carrying multidrug resistant bacteria to colistin by silver. *Proc. Natl. Acad. Sci. U.S.A.* **2022**, *119* (11), e2119417119 10.1073/pnas.2119417119.

(11) Gordon, D. E.; Jang, G. M.; Bouhaddou, M.; Xu, J.; Obernier, K.; White, K. M.; O'Meara, M. J.; Rezelj, V. V.; Guo, J. Z.; Swaney, D. L.; Tummino, T. A.; Huttenhain, R.; Kaake, R. M.; Richards, A. L.; Tutuncuoglu, B.; Foussard, H.; Batra, J.; Haas, K.; Modak, M.; Kim, M.; Haas, P.; Polacco, B. J.; Braberg, H.; Fabius, J. M.; Eckhardt, M.; Soucheray, M.; Bennett, M. J.; Cakir, M.; McGregor, M. J.; Li, Q.; Meyer, B.; Roesch, F.; Vallet, T.; Mac Kain, A.; Miorin, L.; Moreno, E.; Naing, Z. Z. C.; Zhou, Y.; Peng, S.; Shi, Y.; Zhang, Z.; Shen, W.; Kirby, I. T.; Melnyk, J. E.; Chorba, J. S.; Lou, K.; Dai, S. A.; Barrio-Hernandez, I.; Memon, D.; Hernandez-Armenta, C.; Lyu, J.; Mathy, C. J. P.; Perica, T.; Pilla, K. B.; Ganesan, S. J.; Saltzberg, D. J.; Rakesh, R.; Liu, X.; Rosenthal, S. B.; Calviello, L.; Venkataramanan, S.; Liboy-Lugo, J.; Lin, Y.; Huang, X. P.; Liu, Y.; Wankowicz, S. A.; Bohn, M.; Safari, M.; Ugur, F. S.; Koh, C.; Savar, N. S.; Tran, Q. D.; Shengjuler, D.; Fletcher, S. J.; O'Neal, M. C.; Cai, Y.; Chang, J. C. J.; Broadhurst, D. J.; Klippsten, S.; Sharp, P. P.; Wenzell, N. A.; Kuzuoglu-Ozturk, D.; Wang, H. Y.; Trenker, R.; Young, J. M.; Cavero, D. A.; Hiatt, J.; Roth, T. L.; Rathore, U.; Subramanian, A.; Noack, J.; Hubert, M.; Stroud, R. M.; Frankel, A. D.; Rosenberg, O. S.; Verba, K. A.; Agard, D. A.; Ott, M.; Emerman, M.; Jura, N.; von Zastrow,

M.; Verdin, E.; Ashworth, A.; Schwartz, O.; d'Enfert, C.; Mukherjee, S.; Jacobson, M.; Malik, H. S.; Fujimori, D. G.; Ideker, T.; Craik, C. S.; Floor, S. N.; Fraser, J. S.; Gross, J. D.; Sali, A.; Roth, B. L.; Ruggero, D.; Taunton, J.; Kortemme, T.; Beltrao, P.; Vignuzzi, M.; Garcia-Sastre, A.; Shokat, K. M.; Shoichet, B. K.; Krogan, N. J. A SARS-CoV-2 protein interaction map reveals targets for drug repurposing. *Nature* **2020**, *583* (7816), 459-468 10.1038/s41586−020−2286−9.

(12) Gil-Moles, M.; Basu, U.; Büssing, R.; Hoffmeister, H.; Türck, S.; Varchmin, A.; Ott, I. Gold metallodrugs to target coronavirus proteins: Inhibitory effects on the Spike-ACE2 interaction and on PLpro protease activity by auranofin and gold organometallics. *Chem. Eur. J.* **2020**, *26* (66), 15140-15144 10.1002/chem.202004112.

(13) Yuan, S.; Wang, R.; Chan, J. F.; Zhang, A. J.; Cheng, T.; Chik, K. K.; Ye, Z. W.; Wang, S.; Lee, A. C.; Jin, L.; Li, H.; Jin, D. Y.; Yuen, K. Y.; Sun, H. Metallodrug ranitidine bismuth citrate suppresses SARS-CoV-2 replication and relieves virus-associated pneumonia in Syrian hamsters. *Nat. Microbiol.* **2020**, *5*, 1439-1448 10.1038/s41564−020−00802−x.

(14) Li, H.; Yuan, S.; Wei, X.; Sun, H. Metal-based strategies for the fight against COVID-19. *Chem. Commun.* **2022**, *58* (54), 7466-7482 10.1039/D2CC01772E.

(15) Wang, R.; Chan, J. F.; Wang, S.; Li, H.; Zhao, J.; Ip, T. K.; Zuo, Z.; Yuen, K. Y.; Yuan, S.; Sun, H. Orally administered bismuth drug together with N-acetyl cysteine as a broad-spectrum anti-coronavirus cocktail therapy. *Chem. Sci.* **2022**, *13* (8), 2238-2248 10.1039/D1SC04515F.

(16) Yang, N.; Tanner, J. A.; Zheng, B.-J.; Watt, R. M.; He, M.-L.; Lu, L.-Y.; Jiang, J.-Q.; Shum, K.-T.; Lin, Y.-P.; Wong, K.-L.; Lin, M. C. M.; Kung, H.-F.; Sun, H.; Huang, J.-D. Bismuth complexes inhibit the SARS coronavirus. *Angew. Chem. Int. Ed.* **2007**, *46* (34), 6464-6468 10.1002/anie.200701021.

(17) Yang, N.; Tanner, J. A.; Wang, Z.; Huang, J.-D.; Zheng, B.-J.; Zhu, N.; Sun, H. Inhibition of SARS coronavirus helicase by bismuth complexes. *Chem. Commun.* **2007**, (42), 4413-4415 10.1039/b709515e.

(18) Karges, J.; Kalaj, M.; Gembicky, M.; Cohen, S. M. Re(I) tricarbonyl complexes as coordinate covalent inhibitors for the SARS-CoV-2 main cysteine protease. *Angew. Chem. Int. Ed.* **2021**, *60* (19), 10716-10723 10.1002/anie.202016768.

(19) Lemire, J. A.; Harrison, J. J.; Turner, R. J. Antimicrobial activity of metals: mechanisms, molecular targets and applications. *Nat. Rev. Microbiol.* **2013**, *11* (6), 371-384 10.1038/nrmicro3028.

(20) Wang, H.; Wang, M.; Xu, X.; Gao, P.; Xu, Z.; Zhang, Q.; Li, H.; Yan, A.; Kao, R. Y.-T.; Sun, H. Multi-target mode of action of silver against *Staphylococcus aureus* endows it with capability to combat antibiotic resistance. *Nat. Commun.* **2021**, *12* (1), 3331 10.1038/s41467−021−23659−y.

(21) Hammer, S. M.; Katzenstein, D. A.; Hughes, M. D.; Gundacker, H.; Schooley, R. T.; Haubrich, R. H.; Henry, W. K.; Lederman, M. M.; Phair, J. P.; Niu, M.; Hirsch, M. S.; Merigan, T. C. A trial comparing nucleoside monotherapy with combination therapy in HIV-infected adults with CD4 cell counts from 200 to 500 per cubic millimeter. *N. Engl. J. Med.* **1996**, *335* (15), 1081-1090 10.1056/NEJM199610103351501.

(22) van Leth, F.; Phanuphak, P.; Ruxrungtham, K.; Baraldi, E.; Miller, S.; Gazzard, B.; Cahn, P.; Lalloo, U. G.; van der Westhuizen, I. P.; Malan, D. R.; Johnson, M. A.; Santos, B. R.; Mulcahy, F.; Wood, R.; Levi, G. C.; Reboredo, G.; Squires, K.; Cassetti, I.; Petit, D.; Raffi, F.; Katlama, C.; Murphy, R. L.; Horban, A.; Dam, J. P.; Hassink, E.; van Leeuwen, R.; Robinson, P.; Wit, F. W.; Lange, J. M. A. Comparison of first-line antiretroviral therapy with regimens including nevirapine, efavirenz, or both drugs, plus stavudine and lamivudine: a randomised open-label trial, the 2NN Study. *Lancet* **2004**, *363* (9417), 1253-1263 10.1016/S0140−6736(04)15997−7.

(23) Zhang, L.; Lin, D.; Sun, X.; Curth, U.; Drosten, C.; Sauerhering, L.; Becker, S.; Rox, K.; Hilgenfeld, R. Crystal structure of SARS-CoV-2 main protease provides a basis for design of improved α-ketoamide inhibitors. *Science* **2020**, *368* (6489), 409-412 10.1126/science.abb3405.

(24) Newman, J. A.; Douangamath, A.; Yadzani, S.; Yosaatmadja, Y.; Aimon, A.; Brandao-Neto, J.; Dunnett, L.; Gorrie-Stone, T.; Skyner, R.; Fearon, D.; Schapira, M.; von Delft, F.; Gileadi, O. Structure, mechanism and crystallographic fragment screening of the SARS-CoV-2 NSP13 helicase. *Nat. Commun.* **2021**, *12* (1), 4848 10.1038/s41467−021−25166−6.

(25) Bouvet, M.; Imbert, I.; Subissi, L.; Gluais, L.; Canard, B.; Decroly, E. RNA 3'-end mismatch excision by the severe acute respiratory syndrome coronavirus nonstructural protein nsp10/nsp14 exoribonuclease complex. *Proc. Natl. Acad. Sci. U.S.A.* **2012**, *109* (24), 9372-9377 10.1073/pnas.1201130109.

(26) Ogando, N. S.; El Kazzi, P.; Zevenhoven-Dobbe, J. C.; Bontes, B. W.; Decombe, A.; Posthuma, C. C.; Thiel, V.; Canard, B.; Ferron, F.; Decroly, E.; Snijder, E. J. Structure-function analysis of the nsp14 N7-guanine methyltransferase reveals an essential role in Betacoronavirus replication. *Proc. Natl. Acad. Sci. U.S.A.* **2021**, *118* (49), 9372-9377 10.1073/pnas.2108709118.

(27) Imprachim, N.; Yosaatmadja, Y.; Newman, J. A. Crystal structures and fragment screening of SARS-CoV-2 NSP14 reveal details of exoribonuclease activation and mRNA capping and provide starting points for antiviral drug development. *Nucleic Acids Res.* **2023**, *51* (1), 475-487 10.1093/nar/gkac1207.

(28) Otava, T.; Šála, M.; Li, F.; Fanfrlík, J.; Devkota, K.; Perveen, S.; Chau, I.; Pakarian, P.; Hobza, P.; Vedadi, M.; Boura, E.; Nencka, R. The structure-based design of SARS-CoV-2 nsp14 methyltransferase ligands yields nanomolar inhibitors. *ACS Infect. Dis.* **2021**, *7* (8), 2214-2220 10.1021/acsinfecdis.1c00131.

(29) Rona, G.; Zeke, A.; Miwatani-Minter, B.; De Vries, M.; Kaur, R.; Schinlever, A.; Garcia, S. F.; Goldberg, H. V.; Wang, H.; Hinds, T. R.; Bailly, F.; Zheng, N.; Cotelle, P.; Desmaële, D.; Landau, N. R.; Dittmann, M.; Pagano, M. The nsp14/nsp10 RNA repair complex as a pan-coronavirus therapeutic target. *Cell Death Differ.* **2022**, *29* (2), 285-292 10.1038/s41418−021−00900−1.

(30) Canal, B.; McClure, A. W.; Curran, J. F.; Wu, M.; Ulferts, R.; Weissmann, F.; Zeng, J.; Bertolin, A. P.; Milligan, J. C.; Basu, S.; et al. Identifying SARS-CoV-2 antiviral compounds by screening for small molecule inhibitors of nsp14/nsp10 exoribonuclease. *Biochem. J.* **2021**, *478*, 2445-2464 10.1042/BCJ20210198.

(31) Wang, Y.; Hu, L.; Xu, F.; Quan, Q.; Lai, Y. T.; Xia, W.; Yang, Y.; Chang, Y. Y.; Yang, X.; Chai, Z.; Wang, J.; Chu, I. K.; Li, H.; Sun, H. Integrative approach for the analysis of the proteome-wide response to bismuth drugs in *Helicobacter pylori*. *Chem. Sci.* **2017**, *8* (6), 4626-4633 10.1039/C7SC00766C.

(32) Sun, H.; Zhang, Q.; Wang, R.; Wang, H.; Wong, Y.-T.; Wang, M.; Hao, Q.; Yan, A.; Kao, R. Y.-T.; Ho, P.-L.; Li, H. Resensitizing carbapenem- and colistin-resistant bacteria to antibiotics using auranofin. *Nat. Commun.* **2020**, *11* (1), 5263 10.1038/s41467−020−18939−y.

(33) Wang, R.; Lai, T. P.; Gao, P.; Zhang, H.; Ho, P. L.; Woo, P. C.; Ma, G.; Kao, R. Y.; Li, H.; Sun, H. Bismuth antimicrobial drugs serve as broad-spectrum metallo-β-lactamase inhibitors. *Nat. Commun.* **2018**, *9* (1), 439 10.1038/s41467−018−02828−6.

(34) Amporndanai, K.; Meng, X.; Shang, W.; Jin, Z.; Rogers, M.; Zhao, Y.; Rao, Z.; Liu, Z.-J.; Yang, H.; Zhang, L.; O'Neill, P. M.; Samar Hasnain, S. Inhibition mechanism of SARS-CoV-2 main protease by ebselen and its derivatives. *Nat. Commun.* **2021**, *12* (1), 3061 10.1038/s41467−021−23313−7.

(35) Sargsyan, K.; Lin, C.-C.; Chen, T.; Grauffel, C.; Chen, Y.-P.; Yang, W.-Z.; Yuan, H. S.; Lim, C. Multi-targeting of functional cysteines in multiple conserved SARS-CoV-2 domains by clinically safe Zn-ejectors. *Chem. Sci.* **2020**, *11* (36), 9904-9909 10.1039/D0SC02646H..

(36) Lin, S.; Chen, H.; Chen, Z.; Yang, F.; Ye, F.; Zheng, Y.; Yang, J.; Lin, X.; Sun, H.; Wang, L.; Wen, A.; Dong, H.; Xiao, Q.; Deng, D.; Cao, Y.; Lu, G. Crystal structure of SARS-CoV-2 nsp10 bound to nsp14-ExoN domain reveals an exoribonuclease with both structural and functional integrity. *Nucleic Acids Res.* **2021**, *49* (9), 5382-5392 10.1093/nar/gkab320.

(37) Ma, Y.; Wu, L.; Shaw, N.; Gao, Y.; Wang, J.; Sun, Y.; Lou, Z.; Yan, L.; Zhang, R.; Rao, Z. Structural basis and functional analysis of the SARS coronavirus nsp14–nsp10 complex. *Proc. Natl. Acad. Sci. U.S.A.* **2015**, *112* (30), 9436-9441 10.1073/pnas.1508686112.

(38) He, X.; Liao, X.; Li, H.; Xia, W.; Sun, H. Bismuth-induced inactivation of ferric uptake regulator from *Helicobacter pylori*. *Inorg. Chem.* **2017**, *56* (24), 15041-15048 10.1021/acs.inorgchem.7b02380.

(39) Sun, H.; Li, H.; Harvey, I.; Sadler, P. J. Interactions of bismuth complexes with metallothionein(II). *J. Biol. Chem.* **1999**, *274* (41), 29094-29101 10.1074/jbc.274.41.29094.

(40) Xia, W.; Li, H.; Sun, H. Functional disruption of HypB, a GTPase of *Helicobacter pylori*, by bismuth. *Chem. Commun.* **2014**, *50* (13), 1611-1614 10.1039/C3CC47644H.

(41) *IUPAC Stability Constant Database*; Academic Software: Otley, UK, 1997.

(42) Yang, X.; Li, H.; Cheng, T.; Xia, W.; Lai, Y. T.; Sun, H. Nickel translocation between metallochaperones HypA and UreE in *Helicobacter pylori*. *Metallomics* **2014**, *6* (9), 1731-1736 10.1039/C4MT00134F.

(43) Yang, X.; Koohi-Moghadam, M.; Wang, R.; Chang, Y.-Y.; Woo, P. C. Y.; Wang, J.; Li, H.; Sun, H. Metallochaperone UreG serves as a new target for design of urease inhibitor: A novel strategy for development of antimicrobials. *PLoS Biol.* **2018**, *16* (1), e2003887 10.1371/journal.pbio.2003887.

(44) Halime, Z.; Lachkar, M.; Furet, E.; Halet, J.-F.; Boitrel, B. Linear and pre-organized carboxylic acid picket porphyrins as bismuth chelators. *Inorg. Chem.* **2006**, *45* (26), 10661-10669 10.1021/ic061422y.

(45) Ye, Z. W.; Ong, C. P.; Tang, K.; Fan, Y.; Luo, C.; Zhou, R.; Luo, P.; Cheng, Y.; Gray, V. S.; Wang, P.; Chu, H.; Chan, J. F.; To, K. K.; Chen, H.; Chen, Z.; Yuen, K. Y.; Ling, G. S.; Yuan, S.; Jin, D. Y. Intranasal administration of a single dose of a candidate live attenuated vaccine derived from an NSP16-deficient SARS-CoV-2 strain confers sterilizing immunity in animals. *Cell. Mol. Immunol.* **2022**, *19* (5), 588-601 10.1038/s41423−022−00855−4.

(46) Zhou, Y.; Yuan, S.; To, K. K.; Xu, X.; Li, H.; Cai, J. P.; Luo, C.; Hung, I. F.; Chan, K. H.; Yuen, K. Y.; Li, Y. F.; Chan, J. F.; Sun, H. Multiplex metal-detection based assay (MMDA) for COVID-19 diagnosis and identification of disease severity biomarkers. *Chem. Sci.* **2022**, *13* (11), 3216-3226 10.1039/D1SC05852E.

(47) Smilkstein, M. J.; Knapp, G. L.; Kulig, K. W.; Rumack, B. H. Efficacy of oral N-acetylcysteine in the treatment of acetaminophen overdose. *N. Engl. J. Med.* **1988**, *319* (24), 1557-1562 10.1056/NEJM198812153192401.

(48) Summers, S. P.; Abboud, K. A.; Farrah, S. R.; Palenik, G. J. Syntheses and structures of bismuth(III) complexes with nitrilotriacetic acid, ethylenediaminetetraacetic acid, and diethylenetriaminepentaacetic acid. *Inorg. Chem.* **1994**, *33* (1), 88-92 10.1021/ic00079a017.

(49) Halime, Z.; Lachkar, M.; Roisnel, T.; Furet, E.; Halet, J.-F.; Boitrel, B. Bismuth and lead hanging-carboxylate porphyrins: An unexpected homobimetallic lead(II) complex. *Angew. Chem. Int. Ed.* **2007**, *46*, 5120-5124 10.1002/anie.200700543.

(50) Balieu, S.; Halime, Z.; Lachkar, M.; Boitrel, B. Bismuth insertion in functionalized porphyrins: influence of the structure delivering substituted malonic acid groups. *J. Porphyrins Phthalocyanines* **2008**, *12*, 1223-1231 10.1142/S1088424608000601.

(51) Canal, B.; McClure, A. W.; Curran, J. F.; Wu, M.; Ulferts, R.; Weissmann, F.; Zeng, J.; Bertolin, A. P.; Milligan, J. C.; Basu, S.; Drury, L. S.; Deegan, T. D.; Fujisawa, R.; Roberts, E. L.; Basier, C.; Labib, K.; Beale, R.; Howell, M.; Diffley, J. F. X. Identifying SARS-CoV-2 antiviral compounds by screening for small molecule inhibitors of nsp14/nsp10 exoribonuclease. *Biochem. J.* **2021**, *478* (13), 2445-2464 10.1042/BCJ20210198.

(52) Yuan, S.; Chan, J. F. W.; Chik, K. K. H.; Chan, C. C. Y.; Tsang, J. O. L.; Liang, R.; Cao, J.; Tang, K.; Chen, L. L.; Wen, K.; Cai, J. P.; Ye, Z. W.; Lu, G.; Chu, H.; Jin, D. Y.; Yuen, K. Y. Discovery of the FDA-approved drugs bexarotene, cetilistat, diiodohydroxyquinoline, and abiraterone as potential COVID-19 treatments with a robust two-tier screening system. *Pharmacol. Res.* **2020**, *159*, 104960 10.1016/j.phrs.2020.104960.

(53) Yuan, S.; Chan, C. C.; Chik, K. K.; Tsang, J. O.; Liang, R.; Cao, J.; Tang, K.; Cai, J. P.; Ye, Z. W.; Yin, F.; To, K. K.; Chu, H.; Jin, D. Y.; Hung, I. F.; Yuen, K. Y.; Chan, J. F. Broad-spectrum host-based antivirals targeting the interferon and lipogenesis pathways as potential treatment options for the pandemic coronavirus disease 2019 (COVID-19). *Viruses* **2020**, *12* (6), 628 10.3390/v12060628.

For Table of Contents Use Only

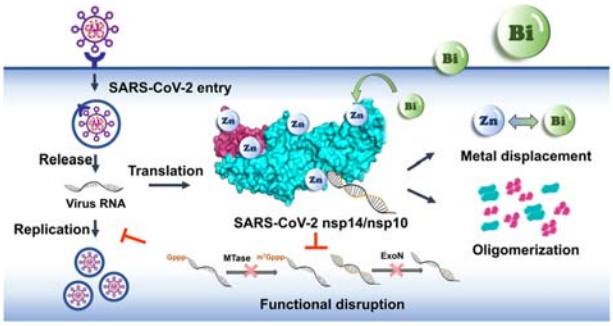

Manuscript title: Development of Pan-Anti-SARS-CoV-2 Agents through Allosteric Inhibition of nsp14/nsp10 Complex

Names of authors: Jingxin Chen, Ying Zhou, Xueying Wei, Xiaohan Xu, Zhenzhi Qin, Chon Phin Ong, Zi-Wei Ye, Dong-Yan Jin, Bernard Boitrel, Shuofeng Yuan, Jasper F.-W. Chan, Hongyan Li*, and Hongzhe Sun*

Brief synopsis: Bi(III)-based compounds can allosterically target at SARS-CoV-2 nsp14/nsp10 complex to disrupt its MTase and ExoN activity, leading to inhibition on SARS-CoV-2 replication in mammalian cells, which is attributable to their ability to displace zinc ions from zinc-finger sites of SARS-CoV-2 nsp14/nsp10 complex by bismuth ions and alter the quaternary structures of the enzymes.